Nucleon excited state wave functions from lattice QCD

Dale S. Roberts, Waseem Kamleh, and Derek B. Leinweber

Special Research Centre for the Subatomic Structure of Matter, School of Chemistry and Physics,
University of Adelaide, South Australia 5005, Australia
(Received 27 November 2013; published 31 March 2014)

We apply the eigenvectors from a variational analysis to successfully extract the three-quark color-singlet wave functions of even-parity excited states of the nucleon. We explore the first four states in the spectrum excited by the standard nucleon interpolating field. We find that the states exhibit a structure qualitatively consistent with a constituent quark model, where the ground, first, second, and third excited states have 0, 1, 2, and 3 nodes in the radial wave function of the d quark about two u quarks at the origin. Moreover, the radial amplitude of the probability distribution is similar to that predicted by constituent quark models. We present a detailed examination of the quark-mass dependence of the probability distributions for these states, searching for a nontrivial role for the multiparticle components mixed in the finite-volume QCD eigenstates. Finally we examine the dependence of the d-quark probability distribution on the positions of the two u quarks. The results are fascinating, with the underlying S-wave orbitals governing the distributions even at rather large u-quark separations.

I. INTRODUCTION

An examination of the three-quark color-singlet wave functions of quarks bound within a hadron provides deep insights into the underlying dynamics of the many-body theory of QCD. It enables a few-body projection of the underlying physics that can be connected with models, shedding light on the essential effective phenomena emerging from the complex dynamics of QCD.

The hadron spectrum is the manifestation of the highly complex dynamics of QCD. It is an observable that is readily accessible in collider experiments. While the quantum numbers of the states can be ascertained, properties providing more insight into the structure of the resonances often remain elusive to experiment. We aim to provide some insight into the underlying dynamics governing the structure of these states.

In quantum field theory, a Schrödinger-like probability distribution can be constructed for bound states by taking a simplified view of the full quantum field theory wave functional in the form of the Bethe-Salpeter wave function [1], herein referred to as simply the "wave function." Recent advances in the isolation of nucleon excited states through correlation-matrix-based variational techniques in lattice QCD now enable the exploration of the structure of these states and how these properties emerge from the fundamental interactions of QCD.

All QCD eigenstates in the finite-volume lattice are superpositions of single and multiparticle states. Their Fock-space structure is complicated, containing the three valence quarks and any number of quark-antiquark pairs, the latter providing overlap with multiparticle components. In calculating a three-quark color-singlet wave function, we are projecting out a single-particle component of this otherwise complicated QCD eigenstate.

In this paper, we extend earlier results [2] focusing on the wave function of the Roper excitation [3] to the four lowest lying even-parity states excited by the standard χ_1 interpolating field which incorporates a scalar diquark construction. Our use of the label Roper for the first even-parity excitation of the nucleon observed in our lattice QCD simulations has a historical context. In constituent quark models, the Roper is identified as the first even-parity excitation of the nucleon. It involves a $2S$ excitation of a quark and displays one node. As we observe this wave function in our lattice simulations, we refer to it as the Roper in the same spirit. However, the large mass of this state observed on the finite-volume lattice makes this reference somewhat controversial, and we discuss this further in the context of our findings.

We begin by examining the quark-mass dependence of the probability distributions for the even-parity states. Here we search for a signature of multiparticle components mixed in the finite-volume QCD eigenstates at the two largest quark masses where the states sit close to the multiparticle thresholds. We also explore the dependence of the d-quark probability distribution on the positions of the two u quarks along an axis through the center of the distribution.

In presenting our results we make extensive use of isovolume and surface plots of the probability distributions for the quarks. Such visualizations have already been used to illustrate physical effects such as Lorentz contraction [4,5], the effect of external magnetic fields [6] and finite volume effects [2,7], for example.

Early explorations of these states were based on nonrelativistic constituent quark models. The probability

distributions of quarks within hadrons were determined using a one-gluon-exchange potential augmented with a confining form [8,9]. These models have been the cornerstone of intuition of hadronic probability distributions for many decades. In this investigation, we confront these early predictions for quark probability distributions in excited states directly via lattice QCD.

In a relativistic gauge theory, the concept of a hadronic wave function is not unique, and the Bethe-Salpeter wave function underlying the probability distributions can be defined in several different forms. For example, the gauge-invariant Bethe-Salpeter amplitude exploits a string of flux to connect the quarks annihilated at different spatial positions in a gauge-invariant manner. As this leads to an explicit path dependence, an average over the paths is desirable. Another approach considers Bethe-Salpeter amplitudes in which the gauge degree of freedom is fixed to a specific gauge. In lattice field theory, Coulomb and Landau gauges are most common due to their local gauge-fixing procedure. The Landau gauge provides distributions that compare favorably with constituent quark model predictions [2], and therefore, we select the Landau gauge herein.

II. LATTICE TECHNIQUES

Robust methods have been developed that allow the isolation and study of the states associated with these resonances in lattice QCD [2,10–20]. In this study, we apply the variational method [21,22] to extract the ground state and first three P_{11} excited states of the proton associated with the Roper [3] and other higher energy P_{11} states. We then combine this with lattice wave-function techniques to calculate the probability distributions of these states at several quark masses and quark positions. We use the $2 + 1$ flavor $32^3 \times 64$ PACS-CS configurations [23] at a pion mass as low as 156 MeV.

The wave function of a hadron is proportional to the parity-projected [24] two-point Green's function,

$$G_{ij}^{\pm}(\vec{p}, t) = \sum_{\vec{x}} e^{-i\vec{p}\cdot\vec{x}} \mathrm{tr}(\gamma_0 \pm 1) \langle \Omega | T\{\chi_i(\vec{x}, t)\bar{\chi}_j(\vec{0}, 0)\} | \Omega \rangle,$$

$$(1)$$

where χ_i are the hadronic interpolating fields. In the case of the proton, the most commonly used interpolator is given by

$$\chi_1(x) = \epsilon^{abc}(u^{\mathsf{T}a}(x)C\gamma_5 d^b(x))u^c(x),$$ (2)

with the corresponding adjoint given by

$$\bar{\chi}_1(0) = \epsilon^{abc}(\bar{d}^b(0)C\gamma_5\bar{u}^{\mathsf{T}a}(0))\bar{u}^c(0).$$ (3)

In order to construct the wave function, the quark fields in the annihilation operator are each given a spatial dependence,

$$\chi_1(\vec{x}, \vec{y}, \vec{z}, \vec{w}) = \epsilon^{abc}(u^{\mathsf{T}a}(\vec{x} + \vec{y})C\gamma_5 d^b(\vec{x} + \vec{z}))u^c(\vec{x} + \vec{w}),$$

$$(4)$$

while the creation operator remains local. This generalizes $G(\vec{p}, t)$ to a wave function proportional to $G(\vec{p}, t; \vec{y}, \vec{z}, \vec{w})$. In principle, we could allow each of these coordinates, $\vec{y}, \vec{z}, \vec{w}$, to vary across the entire lattice; however, we can reduce the computational cost by taking advantage of the hypercubic rotational and translational symmetries of the lattice. A near-complete description of the probability distribution of a particular quark within the proton can be formed by separating two of the quarks along a fixed axis and calculating the third quark's wave function for every lattice site. For this study, we focus on the probability distribution of the d quark from Eq. (4) with the u quarks being separated along the x axis through the center of the distribution, i.e.,

$$\chi_1(\vec{x}, \vec{d}_1, \vec{z}, \vec{d}_2; t) = \epsilon^{abc}(u^{\mathsf{T}a}(\vec{x} + \vec{d}_1, t)$$
$$\times C\gamma_5 d^b(\vec{x} + \vec{z}, t))u^c(\vec{x} + \vec{d}_2, t). \quad (5)$$

where $\vec{d}_i = (d_i, 0, 0)$, $d_1 > 0$, $d_2 = -d_1$ for separations across an even number of lattice sites and $d_2 = -(d_1 - 1)$ for an odd separation. A symmetrized wave function is presented by averaging the wave functions calculated with the interpolating field in Eq. (5) combined with the wave functions produced by the same interpolating field where $d_1 \leftrightarrow d_2$.

Landau gauge is a smooth gauge that preserves the Lorentz invariance of the theory. While the size and shape of the wave function are gauge dependent, our selection of Landau gauge is supported by our results. For example, the ground-state wave function of the d quark in the proton is described accurately by the nonrelativistic quark model using standard values for the constituent quark masses and string tension of the confining potential [2]. Therefore, this gauge provides a foundation for a more comprehensive wave-function examination.

To isolate energy eigenstates, we use the correlation matrix or variational method [21,22]. As we are interested in the wave functions for states at rest, we select $\vec{p} = 0$ in Eq. (1). To ensure that the matrix elements are all $\sim \mathcal{O}(1)$, each element of $G_{ij}(t)$ is normalized by the diagonal elements of $G(0)$ as $G_{ij}(t)/(\sqrt{G_{ii}(0)}\sqrt{G_{jj}(0)})$ (no sum on i or j). Using an average of $\{U\} + \{U^*\}$ configurations which have equal weight in the QCD action, our construction of the two-point functions is real [25,26].

A linear superposition of interpolators $\bar{\phi}^\alpha = \sum_j \bar{\chi}_j u_j^\alpha$ creating state α provides the following recurrence relation:

$$G_{ij}(t_0 + \Delta t)u_j^\alpha = e^{-m_\alpha \Delta t}G_{ij}(t_0)u_j^\alpha, \quad (6)$$

from which right and left eigenvalue equations are obtained

$$[(G(t_0))^{-1}G(t_0 + \Delta t)]_{ij}u_j^\alpha = c^\alpha u_i^\alpha, \qquad (7)$$

$$v_i^\alpha[G(t_0 + \Delta t)(G(t_0))^{-1}]_{ij} = c^\alpha v_j^\alpha, \qquad (8)$$

with $c^\alpha = e^{-m_a\Delta t}$. The eigenvectors for state α, u_j^α and v_i^α provide the eigenstate-projected correlation function

$$G_\pm^\alpha(t) \equiv v_i^\alpha G_{ij}^\pm(t)u_j^\alpha, \qquad (9)$$

with parity $\pm$. The effective mass can then be calculated from the projected two-point functions by $m(t) = \log(G(t)/G(t+1))$. While the effective mass is insensitive to a wide range of parameters [19], we follow Ref. [19] and select t_0 to be two time slices after the source with $\Delta t = 2$.

Different interpolators exhibit different couplings to the proton ground and excited states and hence can be used to construct a variational basis. The limited number of local interpolators restricts the size of the operator basis [10]. To remedy this, we exploit the smearing dependence of the coupling of states to one or more standard interpolating operators in order to construct a larger variational basis where the χ_i and $\bar{\chi}_j$ from Eq. (1) contain a smearing dependence. This method has been shown to allow access to states associated with resonances such as the Roper [2,19] and the $\Lambda(1405)$ [27].

Our approach contrasts alternative approaches where the smearing extent of the fermion sources is fixed at a single level, either through the use of a single source smearing or through a fixed number of Laplacian eigenvectors used in the distillation approach. In this case, a variety of covariant derivative operators are drawn upon to form an effective basis.

Instead, our approach focuses on differences in the smearing extents of the fermion sources and includes unconventionally large smearings. Originally, the motivation was to obtain differing overlaps of excited states with the smeared sources. For example, Fig. 1 of Ref. [19] illustrates the differences in excited-state superpositions obtained with this approach. However, the results presented herein establish that the ability to set up the node structure of these states is key to isolating highly excited states. The results also explain why all but the highest states are robust against variations in the correlation-matrix basis [19].

The nonlocal sink operator used to construct the wave function is unable to be smeared, and hence the standard technique of Eq. (9) cannot be applied. However, Eq. (7) illustrates that it is sufficient to isolate the state at the source using the right eigenvector. Thus, the probability distributions are calculated with each smeared source operator, and the right eigenvectors calculated from the standard variational analysis are then applied in order to extract the individual states of interest.

Our focus on χ_1 in this investigation follows from the results of Ref. [28], where the lowest lying excitation of the
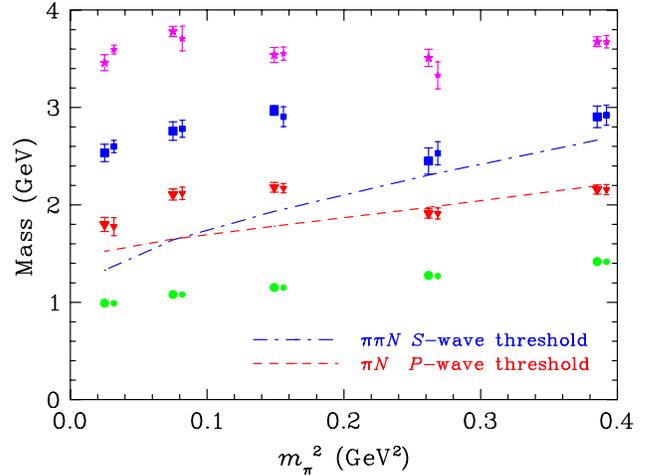

FIG. 1 (color online). The mass dependence of the four lowest lying even-parity eigenstates excited by the χ_1 interpolating field. Results from the 4×4 correlation matrix of χ_1 alone (small symbols offset to the right) are compared with previous results from Ref. [28] obtained from an 8×8 correlation matrix with χ_1 and χ_2 (large symbols offset to the left). These lattice results are compared with the S- and P-wave noninteracting multiparticle energy thresholds on the finite-volume lattice. Plot symbols track the eigenvector associated with each state.

nucleon was shown to be predominantly associated with the χ_1 interpolating field. The results from their 8×8 correlation matrix of χ_1 and $\chi_2 = \epsilon^{abc}(u^{Ta}(x)Cd^b(x)) \times \gamma_5 u^c(x)$ revealed that χ_2 plays a marginal role in exciting the Roper. The coefficients of the Roper source eigenvector multiplying $\bar{\chi}_2$ are near zero. Further comparison with Ref. [28] identifies the third state extracted herein as the fifth state of the 12 states identified and the fourth state herein as the tenth state.

The insensitivity to the size of the correlation matrix when the operators χ_1 and χ_2 are not strongly mixed is illustrated in Fig. 1 presenting the quark-mass dependence of these four states which are examined in detail herein. Results from the 4×4 correlation matrix of χ_1 alone agree with previous results from Ref. [28] obtained from an 8×8 correlation matrix with χ_1 and χ_2.

The quark-mass flow of these states tracked by their associated eigenvectors [28] is not smooth and suggests the presence of avoided level crossings as one transitions from the heaviest two quark masses to lightest three quark masses. At the two heaviest quark masses, it is seems likely these states are dominated by multiparticle $N\pi$ components, whereas at the lighter three quark masses, single-particle components are more dominant. We search for evidence of this in the wave functions of these states.

In summary, the wave function $\psi(\vec{z})$ for the d quark in state number α having momentum $\vec{p}$ observed at Euclidean time t with the u quarks at positions $\vec{d_1}$ and $\vec{d_2}$ is

$$\psi_d^\alpha(\vec{p}, t; \vec{d}_1, \vec{d}_2; \vec{z}) = \sum_{\vec{x}} e^{-i\vec{p}\cdot\vec{x}} \text{tr}(\gamma_0 + 1)$$
$$\times \langle \Omega | T\{\chi_1(\vec{x}, \vec{d}_1, \vec{z}, \vec{d}_2; t)$$
$$\times \bar{\chi}_j(\vec{0}, \vec{0}, \vec{0}, \vec{0}; 0)\} | \Omega \rangle u_j^\alpha, \quad (10)$$

where $\chi_1(\vec{x}, \vec{d}_1, \vec{z}, \vec{d}_2; t)$ is given by Eq. (5).

As discussed above, χ_1 has the spin-flavor construct that is most relevant to the excitation of the Roper from the QCD vacuum. As such, it is an ideal choice for revealing the spatial distribution of quarks within the Roper. However, the selection of χ_1 in Eq. (10) is not unique, and other choices are possible. For example, the selection of χ_2 would reveal small contributions to the Roper wave function where vector diquark degrees of freedom are manifest. Similarly, D-wave contributions could be resolved through the consideration of a spin-3/2 isospin-1/2 interpolating field at the sink. Research exploring these aspects of the wave functions is in progress.

III. SIMULATION RESULTS

A. Lattice parameters

We use the $2 + 1$ flavor $32^3 \times 64$ configurations created by the PACS-CS Collaboration [23] constructed with the Iwasaki gauge action [29] and the $\mathcal{O}(a)$-improved Wilson action [30] with $\beta = 1.90$, giving a lattice spacing of $0.0907(13)$ fm. The hopping parameters are 0.13700, 0.13727, 0.13754, 0.13770, and 0.13781 giving pion masses of 702, 570, 411, 296, and 156 MeV, respectively. For each quark mass we consider 398, 391, 447, 395, and 198 gauge field configurations, respectively, and at the lightest quark mass, we increase statistics through the consideration of four sources per configuration distributed evenly along the time axis.

To isolate the QCD eigenstates, a 4×4 variational basis is constructed using the χ_1 operator with four smearing levels: 16, 35, 100, and 200 sweeps [19] of gauge-invariant Gaussian smearing [31]. These smearing levels correspond to smearing radii of 2.37, 3.50, 5.92, and 8.55 lattice units or 0.215, 0.317, 0.537, and 0.775 fm, respectively.

The choice of variational parameters $t_0 = 2$, $\Delta t = 2$ relative to the source position is ideal, resulting in the effective mass plateaus of the states commencing at $t = t_0 = 2$ as desired [2]. This indicates that the number of states contributing significantly to the correlation functions of the correlation matrix at $t_0 = 2$ equals the dimension of the correlation matrix. As such, we examine the wave functions of all four states with the caution that the fourth state is most susceptible to excited state contamination. In reporting the wave functions, we select the mid point of the correlation matrix analysis at $t = 3$. The wave functions observed for all our states show an approximate symmetry over the eight octants surrounding the origin. To improve our statistics, we average over these eight octants when

$d_1 = d_2 = 0$ and an average over the four quadrants sharing an axis with the u-quark separation at all other values of d_1 and d_2.

We fix to Landau gauge by maximizing the $\mathcal{O}(a^2)$-improved gauge-fixing functional [32]

$$\mathcal{F}_{Imp} = \sum_{x,\mu} \text{Retr}\left(\frac{4}{3} U_\mu(x)\right.$$
$$\left. - \frac{1}{12u_0}(U_\mu(x)U(x+\hat{\mu}) + \text{h.c.})\right) \quad (11)$$

using a Fourier transform accelerated algorithm [33].

In carrying out our calculations, we average over the equally weighted $\{U\}$ and $\{U^*\}$ link configurations as an improved unbiased estimator [25]. The two-point function is then perfectly real, and the probability density is proportional to the square of the wave function. In this analysis, we choose to look at the zero-momentum probability distributions.

B. Wave functions and constituent quark model predictions

Figure 2 presents the wave functions for the first three states at our lightest quark mass providing $m_\pi = 156$ MeV. In the excited states, the wave function changes sign revealing a node structure consistent with $2S$ and $3S$ excited state wave functions. To further explore the details of these wave functions, we construct a probability density from the square of the wave function and plot it on a logarithmic scale in Fig. 3.

Our point of comparison with previous models of quark probability distributions comes from a nonrelativistic constituent quark model with a one-gluon-exchange moti-vated Coulomb-plus-ramp potential. The spin dependence of the model is given in Ref. [9], and the radial Schrödinger equation is solved with boundary conditions relevant to the lattice data obtained in a finite volume with periodic boundary conditions; i.e., the derivative of the wave function is set to vanish at a distance $L_x/2$ from the origin.

We consider standard values of the string tension $\sqrt{\sigma} = 440 \pm 40$ MeV and optimize the constituent quark mass to minimize the logarithmic difference between the quark model and lattice QCD ground-state probability distribu-tions illustrated in the left-hand column of Fig. 3. We find best-fit results for $\sqrt{\sigma} = 400$ MeV, and the optimal con-stituent quark masses range from 340 to 350 MeV over the range of PACS-CS quark masses available. The quark-mass dependence is more subtle than expected and may be associated with the finite volume of the lattice suppressing changes in the wave function as the quark mass is varied. At the lightest quark mass, just above those of nature, the value of 340 MeV is in accord with those traditionally used to describe the hadron spectrum or baryon magnetic moments.
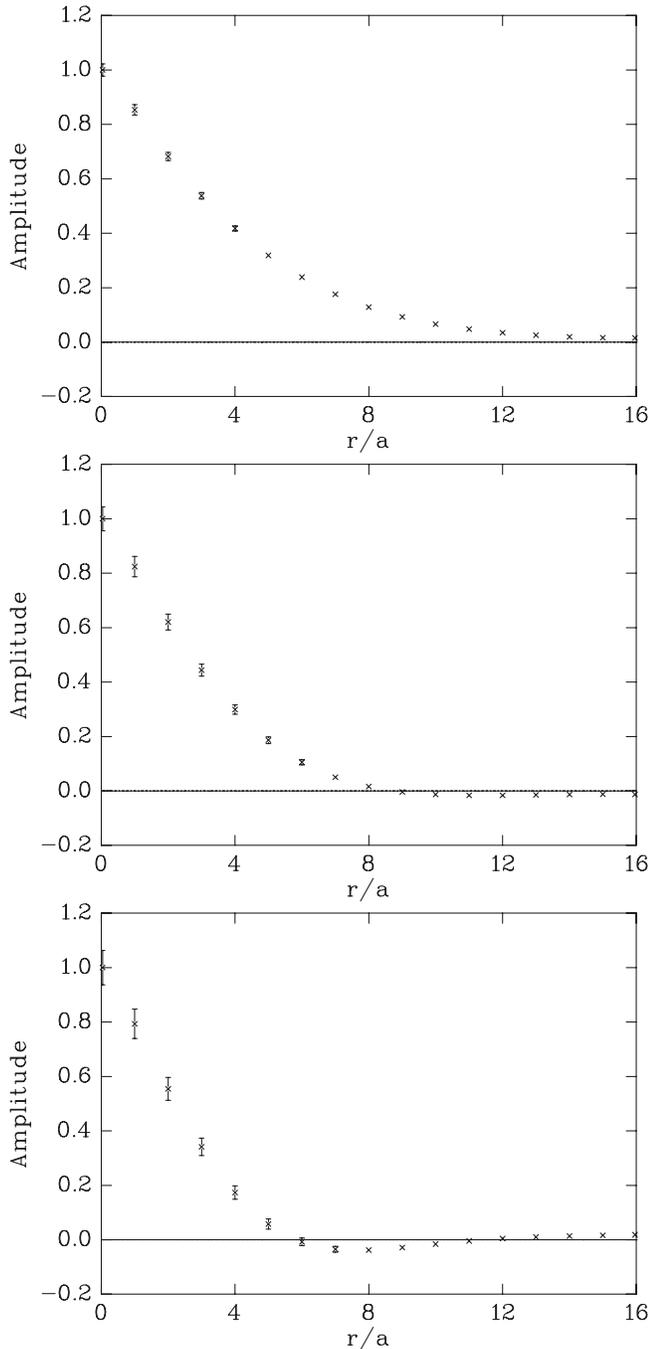
FIG. 2.   The wave function of the d quark in the proton about the two u quarks fixed at the origin for the lightest quark-mass ensemble providing $m_\pi = 156$ MeV. From the top down, the plots correspond to the ground, first, and second excited states observed in our lattice simulation. The wave function changes sign in the excited states and reveals a node structure consistent with $1s$, $2S$, and $3S$ states.

The lattice data for the first three states and all five quark masses are compared with the constituent quark model in Fig. 3. The wave functions are normalized to one at the origin. As the quark model parameters are determined

using only the ground state probability distribution, the probability densities illustrated for the excited states are predictions.

An examination of the left-hand column of Fig. 3 reveals the subtle changes associated with the quark mass. The probability distribution of the heaviest ensemble falls off faster and requires a slightly heavier constituent quark mass to fit the lattice results. This subtle mass dependence is consistent with early, quenched wave-function studies [34].

By comparing the lattice probability distribution for the d quark in the first excited state to that predicted by the constituent quark model in the middle column of Fig. 3, we see a qualitative similarity but with important differences. The quark model predicts the behavior of the lattice wave function very well within the node and predicts the position of the node rather well, particularly at the lightest quark mass. However, the shape of the wave-function tail is very poorly predicted, suggesting an important role for degrees of freedom not contained within the quark model. For example, the long-range pion tail of multiparticle components could alter the distribution of quarks within the state on the lattice. The poorest agreement is for the heaviest ensembles, where the baryon mass is in close proximity to the πN scattering threshold.

Similar comments apply to the second excited state illustrated in the right-hand column of Fig. 3. While the positions of the nodes are predicted approximately, the amplitudes of the wave function between the nodes are very accurately predicted by the quark model. Again, the largest discrepancies are for the heaviest states where the baryon mass is in close proximity to the $\pi\pi N$ scattering threshold.

C. Quark-mass dependence of the probability distributions

1. Ground-state distribution

The mass dependence of the ground-state probability distribution for the d quark about the two u quarks fixed at the origin is illustrated in the two left-hand columns of Fig. 4. The plots are arranged from heaviest to lightest ensembles, with quark mass decreasing down the page.

Although a Gaussian distribution is used to excite the ground state from the vacuum, the well-known sharp-peaked shape associated with the Coulomb potential is reproduced in the probability density for all quark masses. This is best observed in the left-most column where a surface plot reports the probability-density values in the plane containing the two u quarks at the origin.

Because the total probability density is normalized to unity in the spatial volume, the height of the peak drops as the d quark becomes light and moves to larger distances from the u quarks. The surface plot provides the clearest representation of the mass dependence of the ground state.

This gentle broadening of the distribution is also reflected in the isovolume rendering of the projected
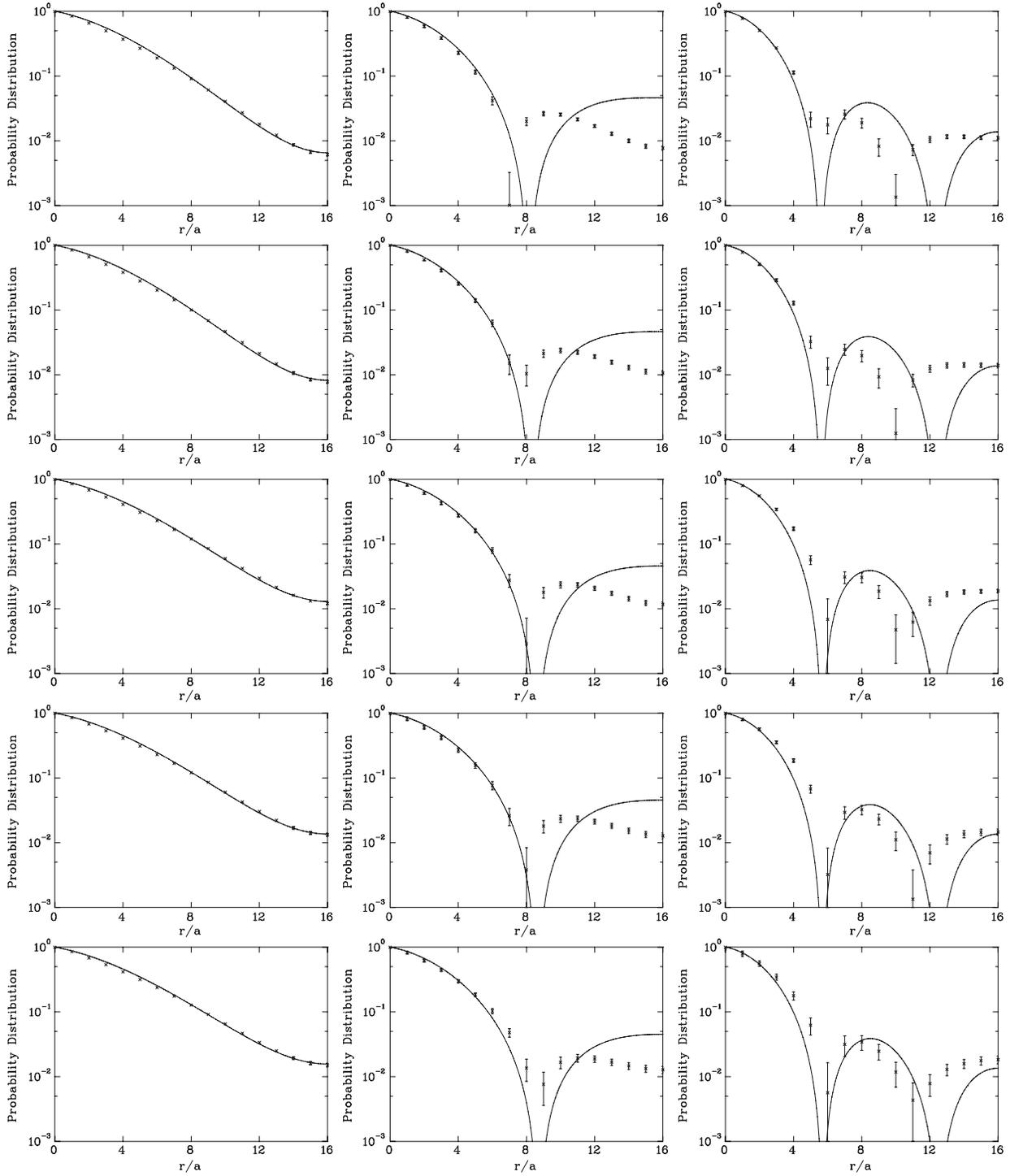
FIG. 3. The probability distributions for the d quark about two u quarks fixed at the origin obtained in our lattice QCD calculations (crosses) are compared with the quark model prediction (solid curve) for the ground (left column), first (middle column), and second (right column) excited states. Quark masses range from the heaviest (top row) through to the lightest (bottom row). The ground state probability distribution of the quark model closely resembles the lattice data for all masses considered. The first excited states matches the lattice data well at small distances, but the node is placed further from the center of mass in the quark model, after which the lattice data show a distinct second peak, whereas the quark model rises to the boundary. It is interesting that the most significant difference is observed where long-distance physics associated with pion-cloud effects not included in the quark model are significant. For the third state, the amplitudes of the shells between the nodes of the wave function are predicted well.
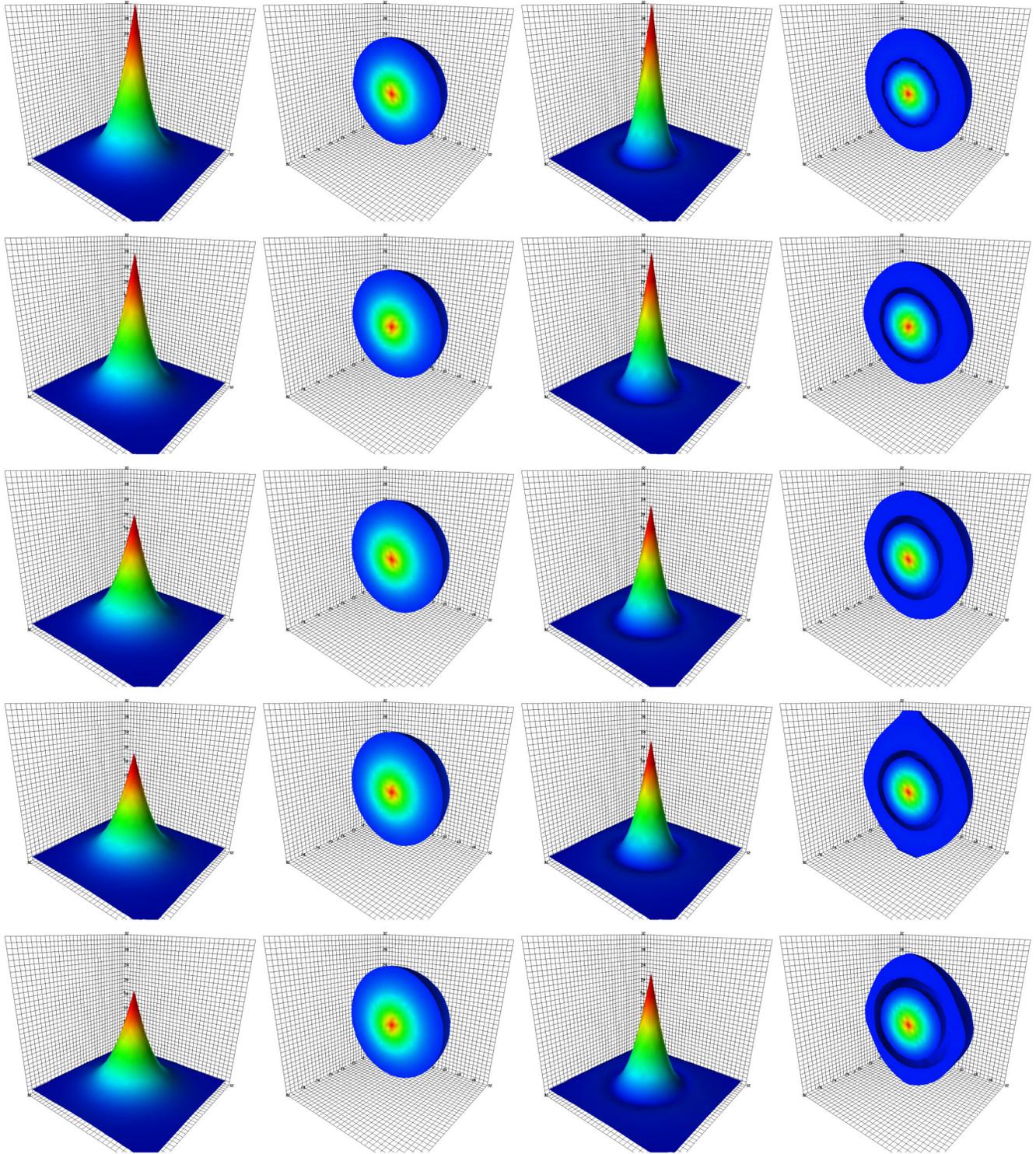
FIG. 4 (color online). The dependence of the d-quark probability distribution on the masses of the quarks in the proton (two left-hand columns) and its first excited state (two right-hand columns). The u quarks are fixed at the origin at the center of the plot. The quark mass decreases from heaviest (top row) to lightest (bottom row). For each mass and state, the probability density is normalized to unity over the spatial volume of the lattice. The isovolume threshold for rendering the probability distribution in the second and fourth columns is 3.0×10^{-5}. The three-dimensional axis grid provides an indication of the positions of the 32^3 lattice sites for the isovolume. The bottom plane of the grid indicates the (z_1, z_2) coordinates of the lattice sites for the surface plots. The PACS-CS scheme for determining the lattice spacing provides a constant lattice spacing for all masses considered with $a = 0.0907(13)$ fm.

ground-state probability density in the second column of Fig. 4. The isovolume has been cut into the plane containing the u quarks at the origin. The threshold for rendering the probability distribution is 3.0×10^{-5}, revealing a smooth sphere for the surface of the probability distribution. The flow of probability-density values is depicted by a color map similar to that used for the surface plot. The colors in the surface and isovolume plots illustrate the flow of data values from the maximum value, rendered in red, to the minimum value, rendered in blue.

Rendering the probability density down to the threshold value of 3.0×10^{-5} does not reveal any significant finite volume effects in the probability densities of the ground state at any of the quark masses considered. This is in spite of the fact that the lightest ensemble has $m_\pi L = 2.23$. As we see, this absence of finite-volume effects is in sharp contrast to all of the excited states examined, and this indicates a nontrivial role for the finite volume in the nucleon mass spectrum.

It is well known that ensembles with $m_\pi L \sim 2$ display significant finite volume effects in the ground-state hadron mass spectrum. These effects can be revealed in the ground-state wave functions by dropping the rendering threshold to lower values. These finite volume effects are examined further in Sec. III D 3.

2. First excited state

Lattice results for the d-quark probability distribution about the two u quarks at the origin in the first excited state of the proton are illustrated in the third and fourth columns of Fig. 4. In the light quark-mass regime, this first excited state is associated with the Roper resonance. The darkened ring around the peak in the surface plot indicates a node in the probability distribution, consistent with a $2S$ radial excitation of the d quark. The node is better illustrated in the isovolume renderings where the probability density drops below the rendering cutoff of 3.0×10^{-5} and leaves a void between the inner and outer shells of the state.

It is interesting that the narrowest distribution is seen at the heaviest quark masses, even though these states have energies coincident with the πN scattering threshold. Enforcing a color-singlet structure in annihilating the three spatially separated quarks prevents a direct observation of the two-particle components contained in the dynamics governing the energy of the state. In this case, the multiparticle components only modify the three-quark distributions.

The outer edge of the isovolume reveals interesting boundary effects which may be associated with the necessary finite-volume effects of multiparticle components mixed in the state. The deviation from spherical symmetry in the outer shell is reflected in the energy of the excited state observed in the finite-volume lattice simulation. At the lightest two quark masses, the distortion of the probability distribution is significant and correspondingly influences

the eigenenergy. Even with $m_\pi L = 4.4$ at the second lightest quark mass, finite volume effects distort the wave function in a significant manner. Of course, this interplay between the finite volume and the energy of the state is key to extracting resonance parameters from lattice simulation results.

The nodal structure of the first excited state also indicates that the ideal combination of operators to access this state on the lattice is a superposition of Gaussian distributions of different widths and opposite signs [19,28]. Figure 5 presents the eigenvectors u_i^α describing the contributions of each of the source smearing levels to the states α for the lightest quark-mass ensemble considered.

For the ground state, all smeared sources contribute positively to the state. There is significant interplay between the smeared sources over the jackknife subensembles giving rise to larger uncertainties for the preferred operators. This is not the case for the excited states where particular superpositions of interpolating fields are required to isolate the states.

For the first excited state, a single large-width Gaussian contributes with a sign opposite to that of a narrower Gaussian, reflecting the wave function illustrated in the second plot of Fig. 2. The combination of sources creating the second excited state has a similar pattern, with a narrow Gaussian contributing positively, an intermediate Gaussian contributing negatively, and a wide Gaussian contributing positively, again reflecting the wave function illustrated in Fig. 2 for this state. This sign-alternating structure is also apparent for the fourth state, suggesting a $3S$ excitation for this state. We examine this state further in the following.
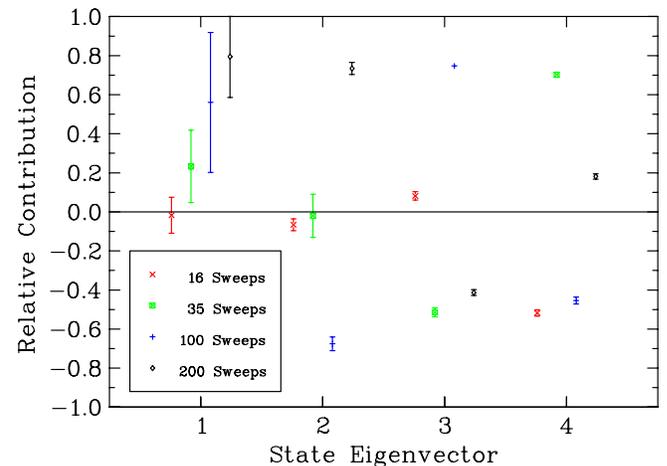

FIG. 5 (color online). The eigenvectors u_i^α describing the contributions of each of the source smearing levels to the states α for the lightest quark-mass ensemble considered. Indices $i = 1$ to 4 correspond to 16, 35, 100, and 200 sweeps of gauge-invariant Gaussian smearing. The superposition of positive and negative Gaussian smearing levels is consistent with the nodal structure recovered in the wave functions.

Turning our attention to the mass dependence of the node we note that the movement is somewhat unusual. While there is a general trend of the node in the wave function moving outward as the quark mass decreases, there is negligible movement in the node between the third and second lightest quark masses. We also note how the width of the void in the probability density increases as the quarks become lighter.

3. Second excitation

The probability distributions for the second excitation of the proton observed in this study are illustrated in the two left-hand columns of Fig. 6. Two nodes are evident at all quark masses, consistent with a $3S$ radial excitation for the d quark. The first inner node is thin at the heavier masses and difficult to see in the isovolume renderings. Finite volume effects are readily observed in the outermost shell.

For the heaviest mass, finite volume effects at the nodes are minimal. The nodes are spherical in shape and are largely unaffected by the boundary. Again there is a trend of the nodes moving further from the center as the quarks become light.

However, it is the middle quark mass considered that has the broadest distribution. The quark-mass flow of the eigenstate energies suggests that avoided level crossings are important between the third and fourth heaviest quark masses. It may be a strong mixing with multiparticle states that is giving rise to the broad distribution of quarks at the middle quark mass.

For the lightest two quark masses the outer node has taken on a squared-off shape, having been distorted by the boundary of the lattice. Again, this is an indication that, even though the ground-state wave function presents as spherical for this quark mass, this excited state is showing clear finite volume effects. Even at relatively modest quark masses, the wave functions of states above the decay thresholds show an important relationship with the finite volume of the lattice.

4. Third excitation

The two right-hand columns of Fig. 6 illustrate the mass dependence of the d-quark probability distribution for the highest excitation of the proton observed in our analysis. As the fourth state of a 4×4 correlation matrix, this state is highly susceptible to contamination from excited states. However, the sign-altering behavior of the interpolator strengths illustrated in Fig. 5 suggests that the correlation matrix has set up the node structure of a $3S$ excitation. Moreover, Fig. 1 of Ref. [19] illustrates how the mass of this state displays only minor sensitivity to the variation of the basis, suggesting that any basis offering a well-spaced range of smearing extents is able to access this state. As one might anticipate, Fig. 6 reveals that the basis is more effective at some quark masses than others. The presence of

three nodes in the wave function is best observed at the heaviest and second lightest quarks masses.

The innermost node is easily observed in the surface plots. However, it is very sharp and does not render in an obvious manner in the isovolume illustrations. The second node is easily rendered, and the third node is very broad. To illustrate this node structure, the outermost shell has become fragmented in the isovolume plots. The fragments reveal the strong finite volume effects on this state.

What is interesting is the manner in which the finite volume effects on the outer shell change as a function of quark mass. At the heaviest quark mass, the outer shell is strongest along the sides of the lattice. By the time one encounters the lightest ensemble, the outer shell has moved to the corners as if there is no longer room for the outer shell along the sides of the 2.9-fm lattice.

D. Discussion

1. Correlation matrix basis

Our correlation matrix basis is founded on the utilization of a variety of smearing extents in constructing the basis. The reason that this approach is effective has now become clear. The smearing extent of the interpolating fields used in constructing a basis can be exploited to set up the node structure of the QCD eigenstates.

As highlighted in Sec. II, the utility of the smearing approach to constructing a correlation matrix basis was originally based on the observation that very different superpositions of excited states are observed in smeared-local correlation functions as the smearing extent of the source is changed. This effect is illustrated in Fig. 1 of Ref. [19]. However, the results presented herein establish that the correlation matrix resolves the QCD eigenstates by setting up the node structure of the wave functions of these states. This is done by superposing Gaussian distributions of increasing widths with a sign-alternating structure, as illustrated in Fig. 5. It will be interesting to complement covariant derivative-based approaches with a variety of smearing extents in constructing larger correlation matrices.

2. The Roper excitation

Turning to our examination of the Roper wave function, we note the large value of 1.8(1) GeV observed for the first even-parity excited state on our finite-volume lattice makes our use of the term Roper somewhat controversial. There are speculations that the Roper is very exotic and that it will not be revealed until the full multiparticle spectrum is understood. In this case, one believes that we have missed the Roper on the lattice and a more comprehensive set of interpolating fields is required to form a basis having strong overlap with the Roper state on the lattice.

An alternative concern is that the large mass of the first excited state observed in our calculation is due to an
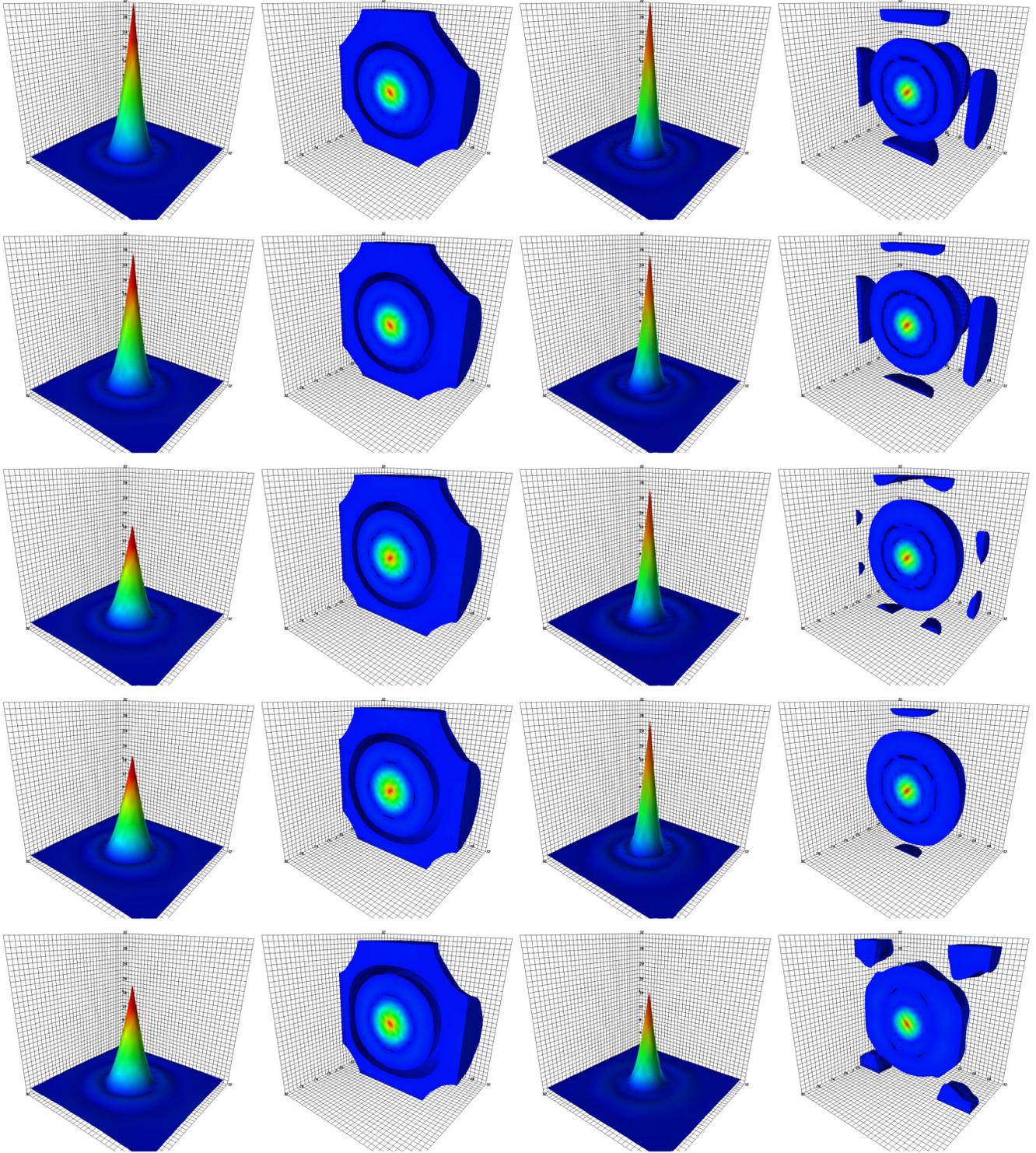
FIG. 6 (color online).   The dependence of the d-quark probability distribution on the masses of the quarks in the proton for the second (two left-hand columns) and third (two right-hand columns) S-wave excited states of the proton observed herein. The u quarks are fixed at the origin at the center of the plot. The quark mass decreases from heaviest (top row) to lightest (bottom row). For each mass and state, the probability density is normalized to unity over the spatial volume of the lattice. The isovolume threshold for rendering the probability distribution in the second and fourth columns is 2.0×10^{-5} and 3.1×10^{-5}, respectively. While the former renders the outer shell coherently, the latter better reveals the node structure of the $3S$ distribution. The three-dimensional axis grid provides an indication of the positions of the 32^3 lattice sites for the isovolume. The bottom plane of the grid indicates the (z_1, z_2) coordinates of the lattice sites for the surface plots. The PACS-CS scheme for determining the lattice spacing provides a constant lattice spacing for all masses considered with $a = 0.0907(13)$ fm.

undetected superposition of states in the projected correlation function that leads to an erroneous mass and wavefunction determination. The idea here is that two-particle pion-nucleon interpolators are key to resolving a single eigenstate in the lattice correlation functions projected in the correlation matrix approach.

Clearly the exploration of multiparticle interpolating fields is central to resolving these issues in an unambiguous manner. However, there is already some evidence suggesting that an alternative explanation of the observed large mass is required.

By carefully monitoring the χ^2 per degree of freedom of the eigenstate-projected correlation functions from the correlation matrix, one can assess the possibility that a second low-lying state is contaminating the projected correlator [35]. In the one case where a second state could be observed in the negative-parity sector, its contribution was suppressed by 2 orders of magnitude and spoiled the single-state-hypothesis energy determination by an amount similar to the statistical uncertainty [35]. For the first even-parity excitation under examination here, the case for extracting a low-lying scattering state is less favorable. An examination of the logarithmic correlation function shows that any contribution from a low-lying scattering state is suppressed by more than 2 orders of magnitude.

While we do not have evidence of a second state contaminating our projected correlators, we do have evidence indicating the dominance of a single state in our first and second excited-state correlators. Our ability to observe a node structure in the first and second excited-state wave functions suggests the dominance of a single state. A superposition with other states would act to hide the node structure.

The same cannot be said for the highest third excited state explored in our analysis. As the highest state extracted from our correlation matrix, this state is the most susceptible to excited-state contamination. The basis we have considered does appear to be effective at the heaviest and second lightest quark masses considered. However, as illustrated in Fig. 6, the node structure is not as apparent at the other quark masses, and this is most likely due to a superposition of states in the correlator masking the node structure.

3. Finite volume effects and the Roper

The large mass for the first even-parity excited state of the nucleon observed at light quark masses herein has a natural explanation as a finite volume effect. As the ensemble with lowest pion mass of 156 MeV has $m_\pi L = 2.23$, such a small volume is known to have significant finite-volume effects even for the ground state [36].

This can be seen in our wave functions by plotting the tail of the probability density. In Fig. 4 we rendered the density for values above the threshold of 3.0×10^{-5}. Dropping the threshold by an order of magnitude to 3.0×10^{-6} provides the isovolume illustrated in Fig. 7. Here the
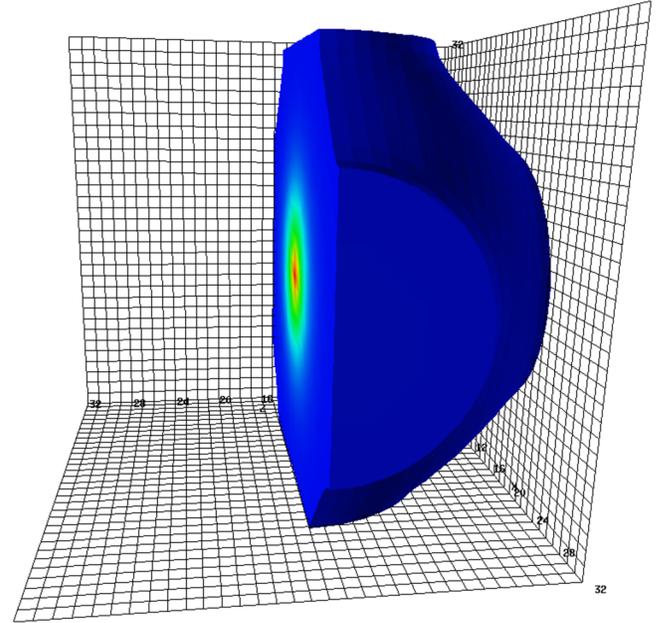

FIG. 7 (color online). The effect of the finite volume of the lattice on the d-quark probability distribution in the proton at the lightest quark mass considered. The u quarks are fixed at the origin at the center of the plot. The isovolume threshold for rendering the probability distribution is an order of magnitude smaller than in Fig. 4 at 3.0×10^{-6}.

deformation of the probability density over all surfaces of the lattice volume is manifest.

Indeed, all of our wave functions for excited states at light quark masses reveal substantial probability density at the spatial boundary with clear boundary effects. This is illustrated in Figs. 4 and 6. This is in accord with the pion-nucleon components of the states gaining amplitude in the light quark-mass regime and the range of the pion cloud increasing as the pion becomes light.

From a finite-volume chiral effective field theory perspective, the main effect of the finite volume is to suppress otherwise important pion self-energy contributions. From the point of view of an effective field theory Hamiltonian approach [37], the excitation spectrum displays a robust volume dependence associated with nonperturbative avoided level crossings and changes in the compositions of the state.

Resolving the nature of this state requires lattice simulations on different and larger volumes with various boundary conditions and multiparticle interpolating fields. By combining these results with the techniques of effective field theory, the evolution of the mass spectrum will be resolved, and the link to nature will be made.

IV. QUARK SEPARATION

In order to investigate a more complete picture of the wave functions of the states isolated herein, we choose to focus on the second-lightest quark-mass ensemble
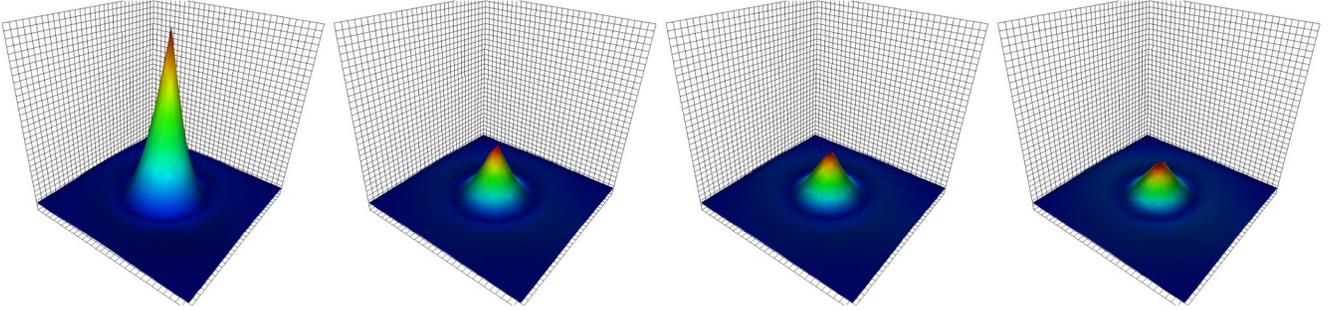
FIG. 8 (color online). The dependence of the d-quark probability distribution on the positions of the u quarks in the first even-parity excited state of the proton at the second lightest quark mass considered. The u quarks are fixed on the x axis running from back right through front left through the center of the plot. The u quarks are fixed a distance of d_1 and d_2 from the origin located at the center. From left to right, the distance $d = d_1 - d_2$ increases, taking values 0, 1, 2, and 3 times the lattice spacing $a = 0.0907$ fm.

providing $m_\pi = 293$ MeV and examine the dependence of the d-quark probability distribution on the positions of the two u quarks composing the states. This mass provides the best compromise between finite-volume effects, quark mass and the ensemble size governing the signal quality and associated uncertainties.

In continuing to investigate the wave function of the d quark, we consider the separation of the u quarks along the x axis, as described in Eq. (5). All integer separations, $d = d_1 - d_2$, between zero and half the lattice extent in the x direction (i.e., 16 lattice units) are considered.

Figure 8 illustrates the probability distribution of the d quark for u quarks separated by 0, 1, 2, and 3 lattice steps in the first excited state associated with the Roper resonance. The most notable feature is the rapid reduction in the overlap of the interpolator with the state as the two u quarks are moved away from the origin. While some broadening of the distribution peak is apparent, it is clear that using a normalization suitable for zero u-quark separation is not effective for illustrating the probability distribution at large u-quark separations.

To better illustrate the underlying shape of the wave functions, the probability distributions are normalized to keep the maximum value of the probability density constant. For small u-quark separations, the center peak height of the distribution is held constant, but for larger separations, the maximum value can be elsewhere in the distribution.

Figure 9 presents the d-quark probability distributions for u-quark separations of $d = 0, 2, 4, 6$, and 8 times the lattice spacing $a = 0.0907$ fm and Fig. 10 completes the study, illustrating u-quark separations of 10, 12, 14, and 16 times the lattice spacing. Each column corresponds to a different state with the ground, first, second, and third excitations illustrated from left to right. The two small spheres above the surface indicate the positions of the two u quarks.

A. Ground-state distribution

Focusing first on the ground state, on separation of the u quarks, the probability distribution of the d quark forms a single broad peak. The structure is slightly rounded until $d = d_1 - d_2 = 12a = 1.09$ fm, with small peaks at the u-quark positions. At a separation of $d = 13a = 1.18$ fm, the wave function takes on a double-peak structure associated with scalar-diquark clustering similar to that illustrated in the third row of Fig. 10 for $d/a = 14$. These results are similar to the earlier quenched wave function results of Refs. [6,34].

B. First excited-state distribution

As the u quarks are separated in the first excited state associated with the Roper, the central peak of the d-quark distribution broadens in a manner similar to that for the ground state. However, by $d = 4a = 0.36$ fm, strength in the wave function is seen to move from the center into the outer shell of the $2S$ state. This transition continues to $d = 10a = 0.91$ fm where the u quarks are still well inside the original node position of the $2S$ distribution. At this point, the central peak has been suppressed, entirely leaving a hole inside the ring or shell in three dimensions. In other words, the node of the wave function has shrunk to the origin. It is interesting how the ringlike probability density is enhanced in the direction perpendicular to the separation of the u quarks.

At $d = 11a = 1.00$ fm, small peaks form in the probability distributions at the positions of the u quarks, revealing the first onset of scalar diquark clustering similar to that in the second row of Fig. 10. At $d = 12a = 1.09$ fm, the u quarks are still within the node of the original wave function, but the radius of the outer shell of the wave function illustrated by the ring in the probability density has reduced slightly. At $d = 14a = 1.27$ fm, the u quarks sit in the node of the original wave function, and there is little memory of the original $2S$ structure. Only a slight swelling at the center of the distribution remains. The central probability density reduces at $d = 15a = 1.36$ fm such that scalar-diquark clustering dominates the probability distribution at $d = 16a = 1.45$ fm.
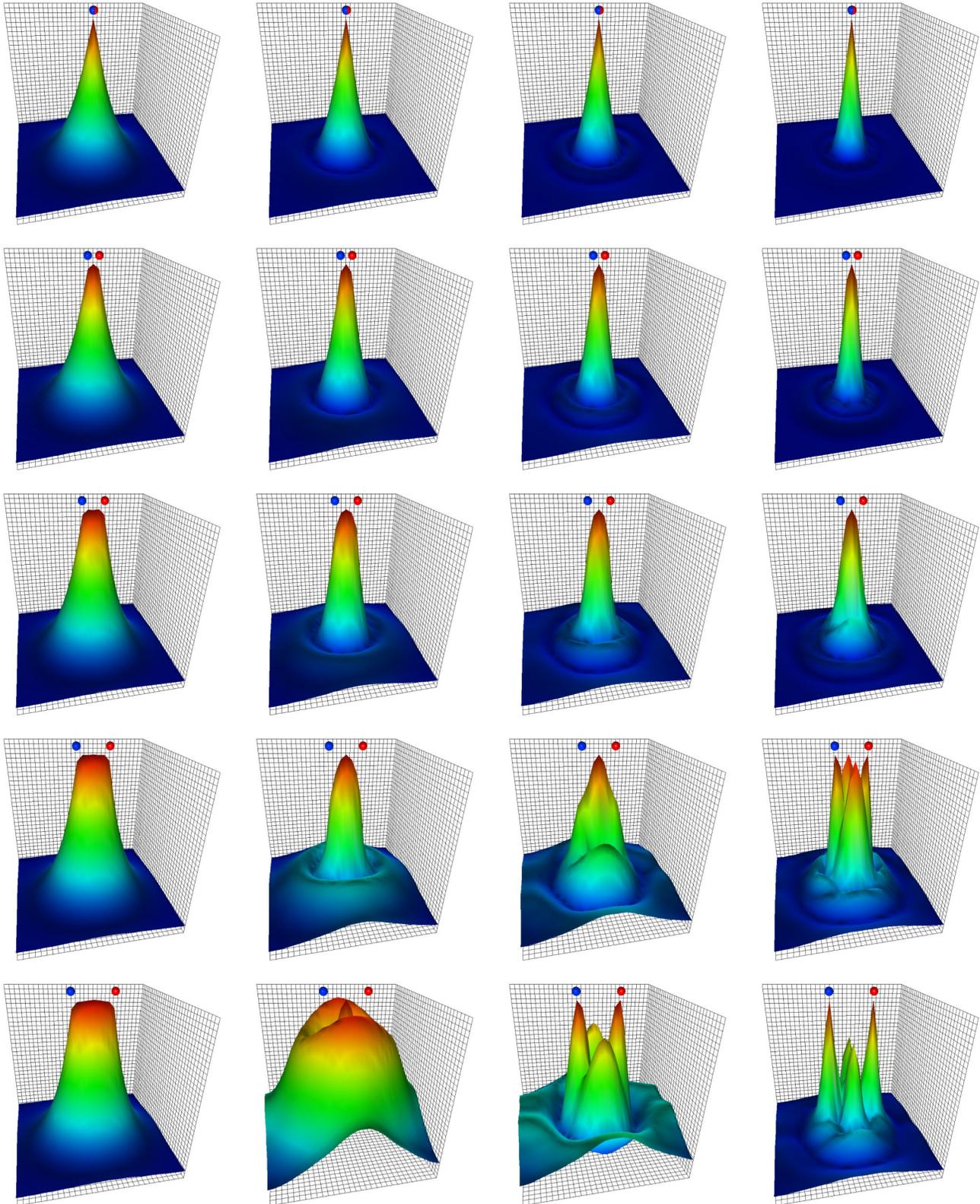
FIG. 9 (color online). The dependence of the d-quark probability distribution on the positions of the u quarks in the proton and its excited states. From left to right, the columns correspond to the ground, first, second, and third S-wave excitations. The u quarks are fixed on the x axis running from back right through front left through the center of the plot. The u quarks are fixed a distance of d_1 and $d_2 = -d_1$ from the origin located at the center. The distance between the quarks, $d = d_1 - d_2$, increases from the top row through to the bottom row, taking values 0, 2, 4, 6, and 8 times the lattice spacing $a = 0.0907$ fm.
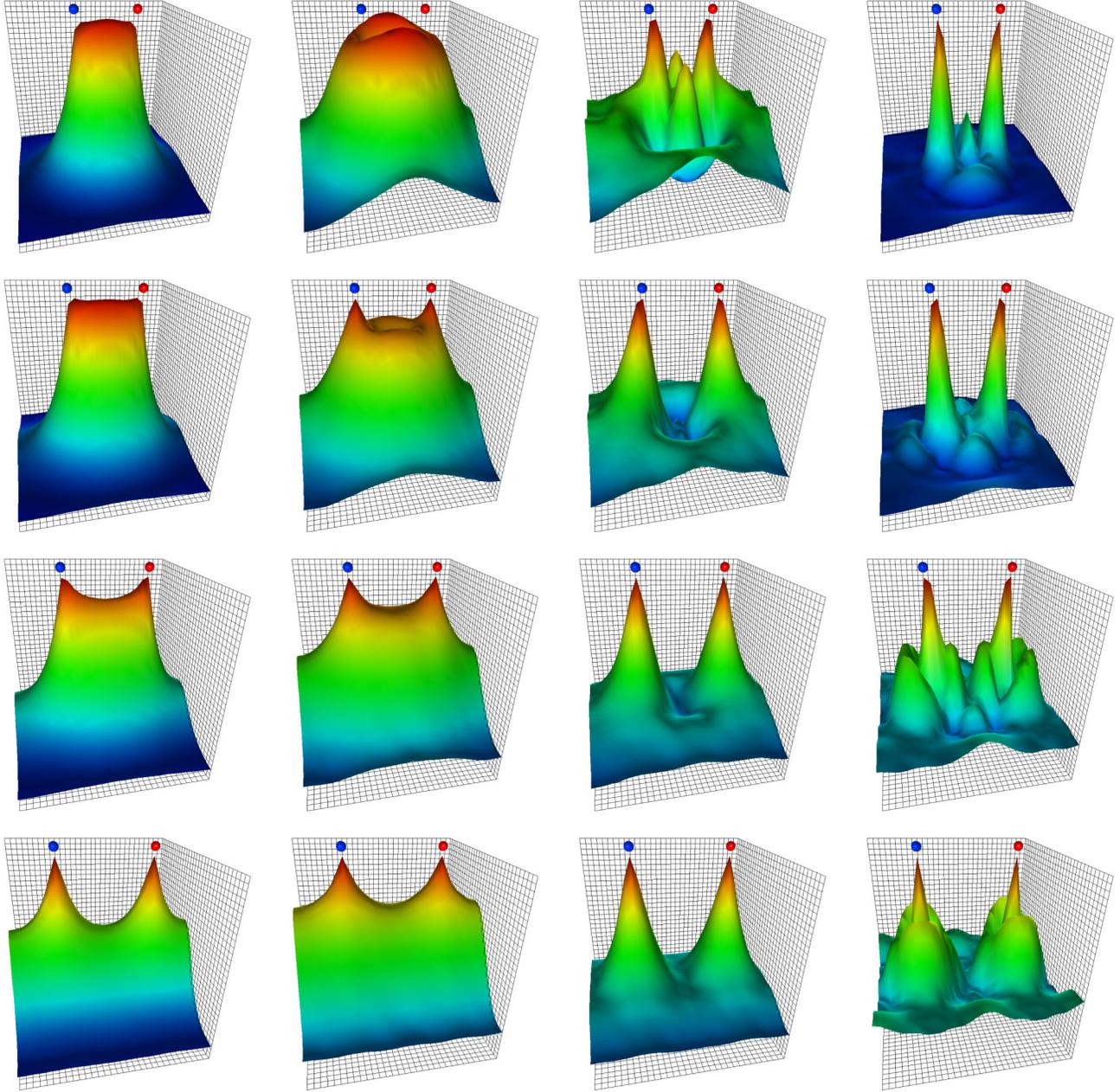
FIG. 10 (color online).   The dependence of the d-quark probability distribution on the positions of the u quarks in the proton and its excited states. From left to right, the columns correspond to the ground, first, second, and third S-wave excitations. The u quarks are fixed on the x axis running from back right through front left through the center of the plot. The u quarks are fixed a distance of d_1 and $d_2 = -d_1$ from the origin located at the center. The distance between the quarks, $d = d_1 - d_2$, increases from the top row through to the bottom row, taking values 10, 12, 14, and 16 times the lattice spacing $a = 0.0907$ fm.

C. Second excitation

For the second excited state observed herein, we again see a shift of the probability density from the central peak to the next shell of the original $3S$-like wave function. At $d = 6a = 0.54$ fm in the fourth row of Fig. 9, a similar enhancement in the first shell is observed as for the Roper at $d = 8a = 0.73$ fm with strength in the probability density enhanced in the direction perpendicular to the separation of the u quarks.

The radius of the first shell about the central peak of the original distribution shrinks as the u quarks are pulled apart, and at $d = 8a = 0.73$ fm corresponding to the bottom row of Fig. 9, the u quarks are now in the first shell where four peaks are apparent. The original first node has shrunk to the center and may have emerged, centered about each of the u quarks. Further evidence of this process is discussed in the analysis of the third excitation below. The second node

of the original wave function now surrounds the four peaks.

The u quarks approach the position of the second node of the wave function at $d = 10a = .91$ fm. The node is still apparent in the front and back of the distribution, orthogonal to the u-quark separation axis. The peaks in the probability distribution are still associated with the first shell surrounding the central peak of the original distribution with zero u-quark separation.

By $d = 12a = 1.09$ fm, the quarks have moved beyond the second node. The radius of node has reduced and can be seen in the dark-blue regions at the center of the plot. At $d = 13a = 1.18$ fm, the second node has collapsed to the origin and explains the strong separation of the two peaks observed at $d = 14a = 1.27$ fm in the third row of Fig. 10. Even at the largest quark separations examined, the node structure of this state is apparent, suppressing the probability density between the two peaks once again governed by scalar-diquark dynamics.

D. Third excitation

The third excitation displays a wonderfully complex structure that mirrors the transitions observed for the first and second excitations for the first few separations. For example, at $d = 4a = 0.36$ fm, one can see the enhancement of the first shell in a direction orthogonal to the u-quark separation axis.

At $d = 6a = 0.54$ fm, a four-peak structure emerges as the u quarks enter the first shell of the wave function. Remarkably, a new nodal structure has emerged. Upon shrinking to the origin, the original first node emerged surrounding each of the peaks at the u-quark positions. This node now cuts through the first shell strength of the underlying $4S$ configuration and divides what would normally be a ring shape into four peaks.

By $d = 10a = 0.91$ fm, the third node surrounds all significant structure in the distribution. The second node has shrunk to surround the small peak in the center, and the first surrounds the u-quark peaks.

At $d = 12a = 1.09$ fm, the third node now surrounds both of the major peaks and the fore and aft humps near the center. The first node continues to surround each of the peaks at the u-quark positions. The emergence of a second node around each of the u quarks is becoming apparent at the left- and right-hand edges of the plot.

At $d = 14a = 1.27$ fm, the third node maintains a circular structure centered about the origin and cuts through the ringlike structures forming around each of the u quarks. The rings clearly reveal the shifting of the first and second nodes to surround each of the u quarks.

At the largest u-quark separation of $d = 16a = 1.45$ fm, the third node has shrunk further to just touch the inside edges of the rings which have formed though the first and second nodes shrinking to the origin and emerging around the two u quarks.

V. CONCLUSIONS

We have examined the three-quark color-singlet single-particle wave functions of even-parity nucleon excitations created in $2 + 1$ flavor lattice QCD simulations. In this first study of the quark probability distribution within excited states of the nucleon, we have shown that all of the states accessed in our correlation matrix analysis display the node structure associated with radial excitations of the quarks. For example, the first excited state associated with the Roper resonance displays a node in the d-quark wave function consistent with a radial excitation of the d quark. The second and third excitations display two and three nodes, respectively.

It is beautiful to observe the emergence of these corner stones of quantum mechanics from the complex many-body theory of quantum field theory. The few-body projection of the underlying physics can be connected with models, shedding light on the essential effective phenomena emerging from the complex dynamics of QCD.

On comparing these probability distributions to those predicted by the constituent quark model, we find good qualitative similarity with interesting differences. The core of the states is described very well by the model, and the amplitudes of the S-wave shells between the nodes are predicted very accurately by the constituent quark model. The discovery of a node structure provides a deep understanding of the success of the smeared-source/sink correlation matrix methods of Ref. [19].

Finite-volume effects are shown to be particularly significant for the excited states explored herein at relatively light quark mass. As these excited states have a multiparticle component, the interplay between the lattice volume, the wave function, and the associated energy are key to extracting the resonance parameters of the states.

Fascinating structure in the d-quark probability distributions of the nucleon excited states is revealed when separating the u quarks from the origin. As the u quarks are separated, the original node structure of the wave function shrinks in size. For example, the Roper reveals a ringed structure in the surface plots corresponding to an empty shell in three dimensions as the node collapses to the origin. The second excited state reveals a four-peaked structure at midrange quark separations. At large separations, these states all display diquark clustering with the d quark most likely found near one of the u quarks. The third state reveals the most exotic structure with new nodes centered about the u quarks appearing after the original nodes collapsed to the origin.

Future calculations explore the structure of these states in more detail, examining the effect of the introduction of isospin-1/2 spin-3/2 interpolating fields [38,39] to reveal the role of D-wave contributions. While our use of improved actions suppresses lattice discretization errors, ultimately simulations will be done at a variety of lattice spacings directly at the physical quark masses. An analysis

of finite-volume effects will also be interesting to further reveal the interplay between the finite volume of the lattice, the structure of the states and the associated energy of the states, thus connecting the lattice QCD simulation results to the resonance physics of nature.

ACKNOWLEDGMENTS

[1] E. E. Salpeter and H. A. Bethe, Phys. Rev. **84**, 1232 (1951).
[2] D. S. Roberts, W. Kamleh, and D. B. Leinweber, Phys. Lett. B, **725**, 164 (2013).
[3] L. D. Roper, Phys. Rev. Lett. **12**, 340 (1964).
[4] M. C. Chu, M. Lissia, and J. W. Negele, Nucl. Phys. **B360**, 31 (1991).
[5] R. Gupta, D. Daniel, and J. Grandy, Phys. Rev. D **48**, 3330 (1993).
[6] D. S. Roberts, P. O. Bowman, W. Kamleh, and D. B. Leinweber, Phys. Rev. D **83**, 094504 (2011).
[7] C. Alexandrou and G. Koutsou, Phys. Rev. D **78**, 094506 (2008).
[8] A. De Rujula, H. Georgi, and S. L. Glashow, Phys. Rev. D **12**, 147 (1975).
[9] R. K. Bhaduri, L. E. Cohler, and Y. Nogami, Phys. Rev. Lett. **44**, 1369 (1980).
[10] D. B. Leinweber, Phys. Rev. D **51**, 6383 (1995).
[11] M. Göckeler, R. Horsley, D. Pleiter, P. E. L. Rakow, G. Schierholz, C. M. Maynard, and D. G. Richards (QCDSF, UKQCD, and LHPC Collaborations), Phys. Lett. B **532**, 63 (2002).
[12] J. Zanotti, S. Bilson-Thompson, F. Bonnet, P. Coddington, D. Leinweber, A. Williams, J. Zhang, W. Melnitchouk, and F. Lee (CSSM Lattice Collaboration), Phys. Rev. D **65**, 074507 (2002).
[13] S. Sasaki, T. Blum, and S. Ohta, Phys. Rev. D **65**, 074503 (2002).
[14] W. Melnitchouk, S. Bilson-Thompson, F. Bonnet, J. Hedditch, F. Lee, D. Leinweber, A. Williams, J. Zanotti, and J. Zhang, Phys. Rev. D **67**, 114506 (2003).
[15] F. X. Lee, S. J. Dong, T. Draper, I. Horvath, K. F. Liu, N. Mathur, and J. B. Zhang, Nucl. Phys. B, Proc. Suppl. **119**, 296 (2003).
[16] D. B. Leinweber, W. Melnitchouk, D. G. Richards, A. G. Williams, and J. M. Zanotti, Lect. Notes Phys. **663**, 71 (2005).
[17] S. Basak, R. Edwards, G. Fleming, K. Juge, A. Lichtl, C. Morningstar, D. Richards, I. Sato, and S. Wallace, Phys. Rev. D **76**, 074504 (2007).
[18] J. Bulava, R. G. Edwards, E. Engelson, B. Joo, H.-W. Lin, C. Morningstar, D. G. Richards, and S. J. Wallace, Phys. Rev. D **82**, 014507 (2010).

[19] M. S. Mahbub, W. Kamleh, D. B. Leinweber, P. J. Moran, and A. G. Williams, Phys. Lett. B **707**, 389 (2012).
[20] M. S. Mahbub, W. Kamleh, D. B. Leinweber, P. J. Moran, and A. G. Williams, Proc. Sci., LATTICE 2011 (**2011**) 127.
[21] C. Michael, Nucl. Phys. **B259**, 58 (1985).
[22] M. Luscher and U. Wolff, Nucl. Phys. **B339**, 222 (1990).
[23] S. Aoki et al. (PACS-CS Collaboration), Phys. Rev. D **79**, 034503 (2009).
[24] F. X. Lee and D. B. Leinweber, Nucl. Phys. B, Proc. Suppl. **73**, 258 (1999).
[25] D. B. Leinweber, R. M. Woloshyn, and T. Draper, Phys. Rev. D **43**, 1659 (1991).
[26] S. Boinepalli, D. B. Leinweber, A. G. Williams, J. M. Zanotti, and J. B. Zhang, Phys. Rev. D **74**, 093005 (2006).
[27] B. J. Menadue, W. Kamleh, D. B. Leinweber, and M. S. Mahbub, Phys. Rev. Lett. **108**, 112001 (2012).
[28] M. S. Mahbub, W. Kamleh, D. B. Leinweber, P. J. Moran, and A. G. Williams, Phys. Rev. D **87**, 094506 (2013).
[29] Y. Iwasaki, arXiv:1111.7054.
[30] B. Sheikholeslami and R. Wohlert, Nucl. Phys. **B259**, 572 (1985).
[31] S. Gusken, Nucl. Phys. B, Proc. Suppl. **17**, 361 (1990).
[32] F. D. R. Bonnet, P. O. Bowman, D. B. Leinweber, A. G. Williams, and D. G. Richards, Aust. J. Phys. **52**, 939 (1999).
[33] C. Davies, G. Batrouni, G. Katz, A. Kronfeld, G. Lepage, K. Wilson, P. Rossi, and B. Svetitsky, Phys. Rev. D **37**, 1581 (1988).
[34] M. W. Hecht and T. A. DeGrand, Phys. Rev. D **46**, 2155 (1992).
[35] M. S. Mahbub, W. Kamleh, D. B. Leinweber, and A. G. Williams, Ann. Phys. (Amsterdam) **342**, 270 (2014).
[36] S. R. Beane, E. Chang, W. Detmold, H. W. Lin, T. C. Luu, K. Orginos, A. Parreño, M. J. Savage, A. Torok, and A. Walker-Loud, Phys. Rev. D **84**, 014507 (2011).
[37] J. M. M. Hall, A. C.-P. Hsu, D. B. Leinweber, A. W. Thomas, and R. D. Young, Phys. Rev. D **87**, 094510 (2013).
[38] J. Zanotti, D. Leinweber, A. Williams, J. Zhang, W. Melnitchouk, and S. Choe (CSSM Lattice Collaboration), Phys. Rev. D **68**, 054506 (2003).
[39] S. Nozawa and D. B. Leinweber, Phys. Rev. D **42**, 3567 (1990).
[40] B. Velikson and D. Weingarten, Nucl. Phys. **B249**, 433 (1985).